Original paper

Schorl-1*A* from Langesundsfjord (Norway)

Fernando CÁMARA[1]*, Ferdinando BOSI[2], Henrik SKOGBY[3], Ulf HÅLENIUS[3], Beatrice CELATA[2], Marco E. CIRIOTTI[4,5]

[1] *University of Milan, via Mangiagalli 34, I-20133 Milan, Italy; fernando.camara@unimi.it*
[2] *Sapienza University of Rome, Piazzale Aldo Moro 5, I-00185, Rome, Italy*
[3] *Department of Geosciences, Swedish Museum of Natural History, Box 50 007, SE-104 05 Stockholm, Sweden*
[4] *Associazione Micromineralogica Italiana, via San Pietro 55, I-10073 Devesi-Cirié, Italy*
[5] *Dipartimento di Scienze della Terra, Università di Torino, via Tommaso Valperga Caluso 35, I-10025 Torino, Italy*
* *Corresponding author*

A crystal fragment of schorl from Langesundsfjord (Norway), showing a zonation with a biaxial optic behavior in the rim, was studied by electron microprobe analysis, single-crystal X-ray diffraction, Mössbauer, infrared and optical absorption spectroscopy and optical measurements. Measured $2V_x$ is 15.6°. We concluded that biaxial character of the sample is not due to internal stress because it cannot be removed by heating and cooling. Diffraction data were refined with a standard *R*3*m* space group model, with a = 16.0013(2) Å, c = 7.2263(1) Å, and with a non-conventional triclinic *R*1 space-group model keeping the same hexagonal triple cell (a = 16.0093(5) Å, b = 16.0042(5) Å, c = 7.2328(2) Å, α = 90.008(3)°, β = 89.856(3)°, γ = 119.90(9)°), yielded R_{all} = 1.75% (3136 unique reflections) *vs.* R_{all} = 2.53% (17342 unique reflections), respectively. The crystal-chemical analysis resulted in the chemical formula $^{X}(Na_{0.98}K_{0.01}\square_{0.01})_{\Sigma1.00}$ $^{Y}(Fe^{2+}_{1.53}Al_{0.68}Mg_{0.35}Ti_{0.20}Fe^{3+}_{0.20}Mn_{0.02}V_{0.01}Zn_{0.01})_{\Sigma3.00}$ $^{Z}(Al_{5.10}Fe^{2+}_{0.50}Mg_{0.40})_{\Sigma6.00}(Si_6O_{18})(BO_3)_3(OH)_3[(OH)_{0.39}F_{0.22}O_{0.39}]_{\Sigma1.00}$, which agrees well in terms of calculated site-scattering (*X* 10.9 *epfu*, *Y* 63.7 *epfu*, *Z* 83.7 *epfu*) and refined site-scattering (*X* 11.4 *epfu*, *Y* 63.4 *epfu*, *Z* 83.6 *epfu*). About 0.19 *apfu* Fe^{2+} is at the *Z* sites in the *R*1 model that showed that one out of six independent *Z* sites (*Z*d) has higher refined site scattering [15.5 *eps vs*. mean 13.7(2) *eps* for the other five sites] and larger mean bond length [1.969 Å *vs*. 1.927(6) Å for the other five sites] and larger octahedral angle variance [53° *vs.* 42(3)°]. All these features support local order of Fe^{2+} at the *Z*d site. Optical absorption spectra also show evidence of Fe^{2+} at the *Z* sites. The elongation of the *Z*d-octahedron is along a direction that forms an angle of ca. 73° with a unit-cell edge and is coincident with the direction of the γ-refraction index. All these data support the triclinic character of the structure of the optically biaxial part of the tourmaline sample from Langesundsfjord and provide evidence that even in the presence of excellent statistical agreement factors from excellent X-ray diffraction data, the lowering of symmetry due to cation ordering may have been overlooked in many other tourmaline samples in the absence of a check of the optical behaviour. According to the nomenclature rules, the studied triclinic schorl, should be named schorl-*1A*.

Keywords: Tourmaline, crystal structure, electron microprobe, Mössbauer spectroscopy, infrared spectroscopy, optical absorption spectroscopy
Received: 14 December 2021; accepted: 17 February 2022; handling editor: J. Cempírek
The online version of this article (doi: 10.3190/jgeosci.344) contains supplementary electronic material.

1. Introduction

It is not uncommon to find references in the literature to anomalous optical behavior in minerals, e.g., birefringence in nominally optically isotropic minerals or the symmetry of optical indicatrix lower than expected for the crystal system of the mineral. For polychrome tourmalines, it has been well known since the 19th century (Madelung 1883; Brauns 1891). Change of refractive index caused by strain (Wertheim 1851, 1854) may be related to structural deformation. Several causes have been suggested for such behavior:

- internal stress arising from defects and compositional heterogeneities ("tourmaline", beryl, "apatite", "garnet", quartz; Foord and Mills 1978); topaz (Isogami and Sunagawa 1975), or by internal stress arising from inclusions (as in diamonds; Howell 2012 and references within) or other minerals (Campomenosi et al. 2020).
- desymmetrization due to order; for example, garnet showing topochemical orthorhombic space group *Fddd* (Takeuchi and Haga 1976) or tetragonal and sector zoning (Hofmeister et al. 1988; Grifen et al. 1992; Andrut et al. 2002; Antao 2013; Cesare et al. 2019). It can also be observed by post-growth order-related phase transitions as for rutile (Foord and Mills 1978) or analcime (Akizuki 1981).
- crystal growth; due to differential incorporation of cations and anions among structurally different sites on the surface that in the bulk crystal are structurally

identical. For example, in elbaite (Hughes et al. 2011) or in elbaite–liddicoatite (Shtukenberg et al. 2007), and in garnet (Akizuki 1984; Allen and Buseck 1988). Internal stress can be released through annealing of the crystal as observed by Foord and Cunningham (1978) in tourmaline from San Diego mine, California, and the process was permanent if the crystal was heated until $2V = 0°$. Similar results were obtained by Hariya and Kimura (1978) in garnet.

As mentioned above, tourmaline samples can show anomalous biaxial behaviour. In 2009, *luinaite-(OH)* was approved (IMA No. 2009-046) with the formula $(Na,\square)(Fe^{2+},Mg)_3Al_6(BO_3)_3Si_6O_{18}(OH)_4$, monoclinic symmetry and *Cm* space group from several different localities. Kolitsch et al. (2011; 2013) reported occurrences of *luinaite-(OH)* and *luinaite-(F)* from the Langesundsfjord area, along with schorl, fluor-schorl, dravite, fluor-elbaite, fluor-liddicoatite and rossmanite, and described it as having *Cm* (monoclinic) that is caused by order of Fe^{3+} and Al^{3+} as a result of the conditions of crystallization.

Kolitsch and co-workers reported high-resolution data ($2\theta = 75°$ MoK_α) and $a = 10.433(2)$, $b = 16.045(3)$, $c = 7.241(1)$ Å, $\beta = 117.61(3)°$ and a refined bulk chemical formula (occupancies of individual split *Y* and *Z* sites were not given): $\sim(Na_{0.94}\square_{0.06})_{\Sigma1.00}(Fe_{2.22}Al_{0.78})_{\Sigma3.00}(Al_{5.10}Fe_{0.90})_{\Sigma6.00}(Si_6O_{18})(BO_3)_3(OH)_3(OH_{0.80}F_{0.20})_{\Sigma1.00}$.

Recently, however, *luinatite-(OH)* has been formally discredited (IMA proposal n. 21-L; Bosi et al. 2022), and any deviation from the reference space group *R*3*m* symmetry should be accommodated in the nomenclature by adding a suffix to the root name that indicates any atypical symmetry (Henry et al. 2011).

2. Sample description

A sample of schorl composition showing a different optical behavior, uniaxial in the dark brownish core and biaxial in the darker brownish rim, coming from Langesundsfjord (Norway), has been studied (GEO-NRM#19252409, Swedish Museum of Natural History). Schorl has been reported by Brøgger (1890) from the wider Langesundsfjord area in the Larvik Plutonic Complex (LPC). Brøgger (1890) noted two main suites of alkaline pegmatites: the Langesundsfjord and Fredriksvärn suites, which contain different HFSE-minerals. Today these are considered as agpaitic and miaskitic mineral assemblages, respectively. The Langesundsfjord suite shows primary complex Na, Zr silicates (Andersen et al. 2010). A 36 µm section was cut perpendicular to **c**-axis. Conoscopic images (Fig. 1) showing uniaxial behavior in the lighter core of the section and biaxial behavior with the negative optic sign were obtained in the darker rims. The biaxial character of the sample is not due to internal stress because it could not be removed by heating and cooling, as observed in tourmaline samples from the San Diego mine (California) by Foord and Cunningham (1978).

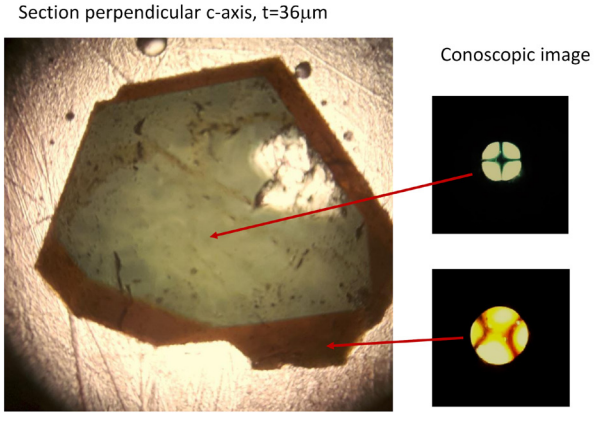

Fig. 1a – Image of the crystal cut perpendicular to **c**-axis and the interference images obtained at the core and the rim of the section.

3. Experimental methods

3.1. Optical measurements

Optical measurements were done with a Supper Co. spindle stage in a Leitz Dialux microscope equipped with a CMOS camera using the Excelibr spreadsheet (Steven and Gunter 2018). A portion corresponding to the dark biaxial rim was first measured, giving $2V_x = 15.6°$ (in white light). The orientation of the optical indicatrix was obtained using the same crystal mounted on a Rigaku XtaLAB Synergy-S diffractometer (MoK_α): **c** ^ *X* = 2°, **b** ^ *Z* = 164.3° and **a** ^ *Z* = 75.8°.

3.2. Electron MicroProbe Analysis (EMPA)

Electron microprobe analysis on the rim and core of the tourmaline crystal, was done using a wavelength-dispersive spectrometer (WDS mode) with a Cameca SX50 instrument at the Istituto di Geologia Ambientale e Geoingegneria, CNR, Rome, Italy. The following analytical conditions were used: accelerating voltage 15 kV, beam current 15 nA and beam diameter of 10 µm. Minerals and synthetic compounds were used as standards: wollastonite (Si, Ca), magnetite (Fe), rutile (Ti), corundum (Al), vanadinite (V), fluorophlogopite (F), periclase (Mg), jadeite (Na), orthoclase (K), sphalerite (Zn), rhodonite (Mn), metallic Cr and Cu. The PAP routine was applied (Pouchou and Pichoir 1991). Results are reported in Tab. 1. Calcium, Cr and Cu were below detection limits (< 0.03 wt. %).

3.3. Mössbauer spectroscopy

Mössbauer spectroscopy was used to determine the $Fe^{3+}/\Sigma Fe$ ratio of the sample, using a conventional spectrometer system operated in constant-acceleration mode. An absorber was prepared from 12 mg sample material obtained from the core region of a crystal that was mixed with an acrylic resin and pressed to a 12-mm diameter disc under mild heating (< 150 °C). Spectra were collected over 1024 channels in the velocity range –4.2 to +4.2 mm/s using a ^{57}Co rhodium matrix standard source of 50 mCi nominal activity. The raw spectrum was folded and calibrated against an α-Fe foil. The spectrum (Fig. 2) was fitted using the software MossA (Prescher et al. 2012) with four doublets assigned to Fe^{2+} and one doublet assigned to Fe^{3+}, resulting in an $Fe^{3+}/\Sigma Fe$ ratio of 0.13 (Tab. 2).

Tab. 1 Average chemical compositions of the rim and core of the tourmaline crystal from Langesundsfjord, Norway.

	rim (n = 10)	core (n = 20)		rim	core
SiO_2[a] (wt. %)	34.55(9)	34.67(22)	Si (*apfu*)	6.000	6.000
TiO_2	1.59(8)	0.39(10)	Ti^{4+}	0.207	0.051
B_2O_3[b]	10.01	10.05	B	3.000	3.000
Al_2O_3	28.22(35)	30.04(43)	Al	5.777	6.128
V_2O_3	0.08(2)	0.04(2)	V^{3+}	0.011	0.006
FeO_{tot}	15.29(31)	14.67(19)			
MnO	0.16(4)	0.14(2)	Mn^{2+}	0.023	0.021
MgO	2.92(7)	2.58(6)	Mg	0.755	0.664
ZnO	0.05(5)	0.05(4)	Zn	0.007	0.007
Na_2O	2.90(5)	2.88(5)	Na	0.975	0.967
K_2O	0.04(2)	–	K	0.009	–
F	0.41(4)	0.16(9)	F	0.224	0.089
H_2O[b]	2.93	2.96	(OH)	3.393	3.420
O = F	–0.17	–0.07			
FeO	13.93[c]	12.67[d]	Fe^{2+}	2.023	1.834
Fe_2O_3	1.512[c]	2.22[d]	Fe^{3+}	0.198	0.289
Total	99.112	98.79			

Notes: Errors for oxides and fluorine are standard deviations (in parentheses) of n spot WDS analyses; *apfu* = atoms per formula unit, normalized to 31 anions (see text).

[a] SiO_2 assumed to equal 6.000 *apfu*. The SiO_2 average value measured in the rim and core of tourmaline crystal are 34.81 wt. % and 35.09 wt. %, respectively.

[b] By stoichiometry

[c] By Optical absorption spectroscopy

[d] By Mössbauer spectroscopy

3.4. Infrared and Optical Absorption Spectroscopy

Fourier-transform infrared spectroscopy (FTIR) was used to characterize the fundamental (OH) vibrational absorption bands in the range 3000–4000 cm^{-1} (Fig. 3). The spectrometer system consisted of a Bruker Vertex 70 spectrometer equipped with a halogen-lamp source and CaF_2 beam-splitter, coupled to a Hyperion II IRmicroscope equipped with a ZnSe wire-grid polarizer and an InSb detector. Polarized absorption spectra were acquired on two differently oriented crystal sections; one cut parallel to the **c**-axis with a thickness of 45 μm (Fig. 1), and one cut perpendicular to the **c**-axis with a thickness of 36 μm (Fig. 4 and 5). The spectra were measured over the wavenumber range 2000–12000 cm^{-1} with a resolution of 4 cm^{-1}, with the measuring area masked by a rectangular 75 × 100 μm aperture.

Polarized room-temperature optical absorption spectra in the range 30000–5000 cm^{-1} (333–1000 nm) were recorded at a spectral resolution of 1 nm on the same 45 μm

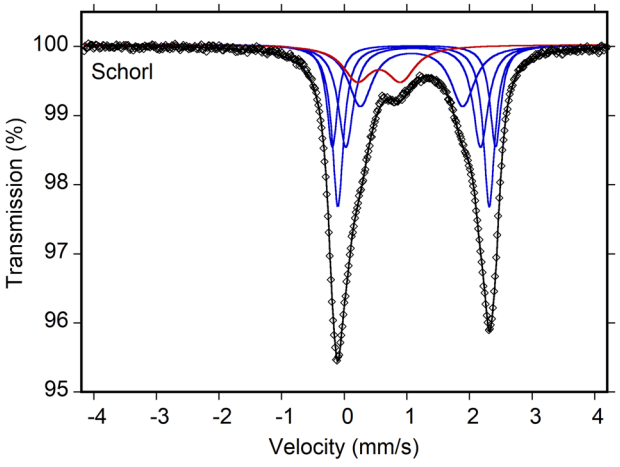

Fig. 2 ^{57}Fe Mössbauer spectrum (core region) obtained at room temperature. Fitted absorption doublets assigned to Fe^{2+} and Fe^{3+} are indicated in blue and red, respectively. Diamonds denote measured spectrum, and the black curve represents summed fitted doublets.

Tab. 2 Mössbauer parameters obtained at room temperature.

d (mm/s)	ΔE_Q (mm/s)	*FWHM* (mm/s)	Area (%)	Assignment
1.11	2.61	0.21	16.4	$^{VI}Fe^{2+}$
1.10	2.42	0.22	26.3	$^{VI}Fe^{2+}$
1.10	2.15	0.30	22.7	$^{VI}Fe^{2+}$
1.07	1.64	0.46	21.0	$^{VI}Fe^{2+}$
0.55	0.70	0.54	13.6	$^{VI}Fe^{3+}$

d = centroid shift, ΔE_Q = quadrupole splitting, *FWHM* = full width at half-maximum.

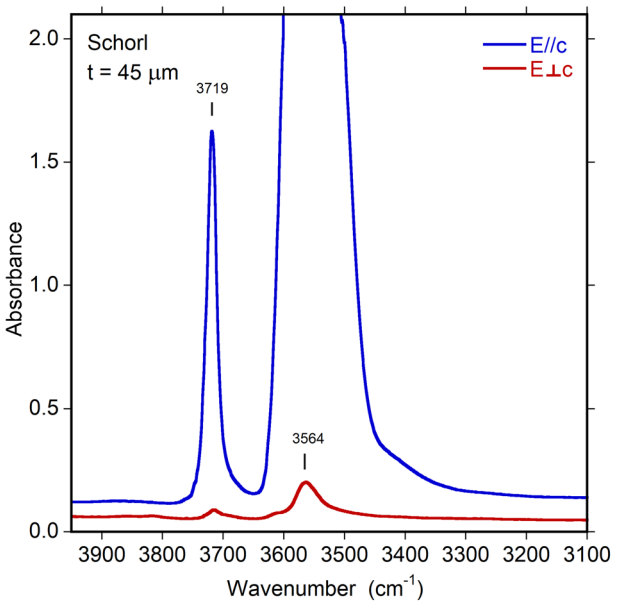

Fig. 3 Polarized FTIR spectra (core region), vertically off-set for clarity. The main band is truncated around 2 absorbance units in the **E** || **c** direction due to excessive absorption. Sample thickness 45 µm.

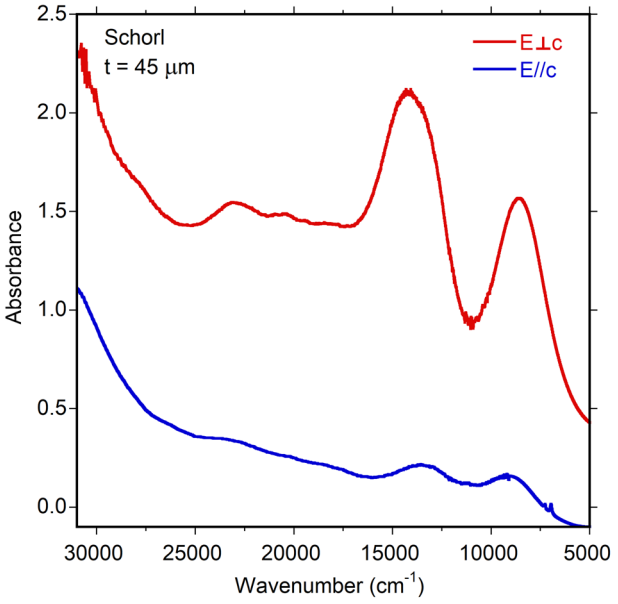

Fig. 4 Polarized optical absorption spectra of the core of a 45 µm thick single crystal cut parallel to the **c**-axis.

thick single crystal section, cut along the **c**-axis, that was studied by FTIR spectroscopy. Spectra of the differently coloured core and rim regions (Fig. 5) were measured on a 36 µm thick crystal section cut perpendicular to the **c**-axis. All spectra were recorded using an AVASPEC-ULS2048×16 spectrometer (Swedish Museum of Natural History, Stockholm, Sweden) attached via a 400 µm UV fiber cable to a Zeiss Axiotron UV-microscope. A 75 W Xe arc lamp was used as a light source, and Zeiss Ultrafluar 10× lenses served as objective and condenser. The

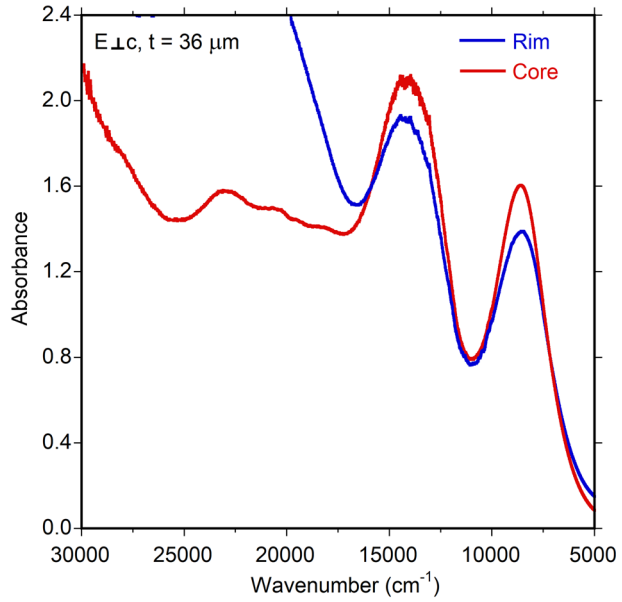

Fig. 5 Polarized optical absorption spectra of the core and rim of a 36 µm thick single crystal cut perpendicular to the **c**-axis. Spectra were recorded at core and rim positions indicated by arrows in Fig. 1.

diameter of the circular measure apertures was in the range 50–75 µm. A UV-quality Glan–Thompson prism with a working range from 40000 to 3704 cm^{-1} (250 to 2700 nm) was used as a polarizer. The wavelength scale of the spectrometer was calibrated against Ho_2O_3-doped and Pr_2O_3/Nd_2O_3-doped standards (Hellma glass filters 666F1 and 666F7). Spectral data in the range 10000–5000 cm^{-1} (1000–2000 nm) was taken from the FTIR measurements.

3.5. Single-crystal X-ray diffraction

A Single-crystal X-ray Structure REFinement (SREF) study was done on a crystal fragment (0.020 × 0.123 × 0.303 mm) from the optically biaxial rim and extracted from a thin section of a tourmaline crystal perpendicular to the prism length. The thin fragment was glued to a glass fibre and mounted on a Rigaku XtaLAB Synergy diffractometer equipped with a Hybrid Pixel Array Detector, using graphite-monochromatized MoK_α radiation (λ = 0.71073 Å); experimental conditions were 50 kV and 1 mA and the detector-to-sample distance was 6.2 cm. A combination of 44 ω scans at different values of and ϕ, χ angles as well as different detector positions at several θ values, with step scan 1°, was used to collect 5039 images to achieve a complete scan of the reciprocal space up to a resolution of 0.50 Å. Exposure time was 10 s per frame at the low θ setting and 22 s at the high θ setting of the detector. The strategy was meant to obtain a complete dataset of high-resolution data allowing for refinement in the point group 1.

The crystal structure was refined starting from a tourmaline *R*3*m* structure model by Hughes et al. (2011). Neutral-atoms scattering curves from The International Tables (Wilson 1992) were used for all the atom positions keeping full fixed occupancy for *T*, *B* and anion sites [but for the O1 (≡ W) and O3 (≡ V) sites] and occupancies were refined at the *X*, *Y* and *Z* cation sites refining relative occupancy of Fe and Al for each type of site, and for the O1 sites refining relative occupancies of O versus F. Hydrogen atoms bonded to O3 site were observed in Fourier-difference maps and were added to the model refining atom coordinates and constraining the isotropic displacement to be 20 % higher than the equivalent isotropic value at the O3 site. Refinement was done with SHELXTL (Sheldrick 2015) with anisotropic-displacement parameters for all non-hydrogen atoms, and the structure was refined on F^2. At convergence, the discrepancy factor was $R_1 = 0.017$ for 3079 unique reflections with $F_o > 4\ \sigma(F)$ and $R_1 = 0.018$ for all 3136 reflections. For the triclinic model, starting coordinates were taken from the tourmaline *R*1 structure model of Hughes et al. (2011), using the same approach as described above. At convergence, hydrogen atoms bonded to the oxygen at the O3 sites were observed in Fourier-difference maps and were added to the model. The model refined to discrepancy factors of $R_1 = 0.023$ for 16304 unique reflections with $F_o > 4\ \sigma(F)$ and $R_1 = 0.025$ for all 17342 reflections.

Tab. 3 Crystal data and experimental conditions for single-crystal XRD study.

Crystal system	Triclinic	Trigonal
Space group	*R*1	*R*3*m*
Unit cell dimensions	a = 16.0093(5) Å	16.0013(2) Å
	b = 16.0042(5) Å	
	c = 7.2328(2) Å	7.22630(10) Å
	α = 90.008(3)°	
	β = 89.856(3)°	
	γ = 119.90(9)°	
Unit cell volume (Å^3)	1606.6(13)	1602.35(5)
Z	3	3
Absorption coefficient	2.36 mm^{-1}	2.36 mm^{-1}
F(000)	1526	1526
Theta range for data collection	2.54 to 44.93°	2.54 to 44.93°
Index ranges	$-31 \le h \le 31$, $-31 \le k \le 31$, $-14 \le l \le 14$	$-31 \le h \le 31$, $-31 \le k \le 31$, $-14 \le l \le 14$
Reflections collected	86725	86725
Independent reflections	17342 [R_{int} = 0.0408]	3136 [R_{int} = 0.0662]
Refinement method	Full-matrix least-squares on F^2	Full-matrix least-squares on F^2
Extinction coefficient	0.00029(7)	0.00055(13)
Flack parameter	0.003(4)	0.029(5)
Data / restraints / parameters	17342 / 3 / 474	3136 / 1 / 95
Goodness-of-fit on F^2	0.974	1.069
Final R indices [$I>2\sigma(I)$]	R_1 = 0.023, wR_2 = 0.047	R_1 = 0.017, wR_2 = 0.040
R indices (all data)	R_1 = 0.025, wR_2 = 0.047	R_1 = 0.018, wR_2 = 0.040
Largest diff. peak and hole (eÅ^{-3})	0.937 and –0.827	0.837 and –0.832

Experimental details, unit-cell parameters and statistical indices for both *R*1 and *R*3*m* models are given in Tab. 3. Fractional atom coordinates, site occupancies, isotropic-displacement parameters and weighted bond-valence sums (using the parameters of Gagnè and Hawthorne 2015) are reported in Tab. 4. Bond distances are given in Tab. 5. A crystallographic information file (CIF) containing observed structure factors has been deposited as Supplementary material.

4. Results

4.1. Infrared and Optical Absorption Spectroscopy

Infrared spectra in the 3100–4000 cm^{-1} region (Fig. 3) show two prominent bands related to O–H stretching modes at 3564 and 3719 cm^{-1}, and a weak shoulder feature around 3420 cm^{-1}. As typically observed for infrared spectra of tourmalines, the (OH) bands are strongly polarized parallel to the **c**-axis, with the main band off-scale due to excessive absorption. The relatively strong band at 3719 cm^{-1}, which occurs in the region where bands due to (OH) at the O1 site (≡ W) are expected, indicates a significant amount of ^{W}(OH). This band is likely caused by the occurrence of the atomic arrangements ^{Y}[Fe^{2+}Fe^{2+}(Fe^{2+},Al)]–^{O1}(OH)–^{X}(Na), based on the studies of Watenphul et al. (2016) and Bosi et al. (2016). Conversely, the band at 3564 cm^{-1} and the shoulder at 3420 cm^{-1} are related to the presence of (OH) groups at the O3 site (≡ V) (e.g., Gonzalez-Carreño et al. 1988; Bosi et al. 2015a).

The optical absorption spectra (Fig. 4 and Fig. 5) show strong and broad absorption bands at 22700, ~14000 and ~9000 cm^{-1}, which are strongly polarized in **E** ⊥ **c** (Fig. 4). In addition, weak and relatively narrow absorption bands occur at 20600 and 18000 cm^{-1}. The relatively broad absorption bands at ~14000 and 9000 cm^{-1} are assigned to Fe^{3+}-enhanced spin-allowed *d*–*d* transitions in six-coordinated Fe^{2+} in accord with previous optical studies of tourmaline (e.g., Mattson and Rossman 1987). Each of these two absorption bands shows a distinct shoulder, which indicates that they are composed of two partly overlapping absorption bands. In detail, the higher energy band shows two-band com-

Tab. 4 Site occupancy (s.o.), atom coordinates and equivalent isotropic displacement parameters (Å^2). Equivalent displacement parameter, U_{eq}, is defined as one third of the trace of the orthogonalized U^{ij} tensor. Bond valence (B.V.S.) in valence units (*v.u.*).

Site *R*1	Atom	*s.o.*	*x/a*	*y/b*	*z/c*	U_{eq}	*B.V.S.*
X	Na	1.037(5)	0.00028(7)	0.00024(7)	0.25347(12)	0.0271(3)	0.889
*Si*a	Si	1	0.85754(3)	0.52376(3)	0.35224(5)	0.00580(6)	4.018
*Si*b	Si	1	0.66345(3)	0.52318(3)	0.35089(5)	0.00584(6)	4.030
*Si*c	Si	1	0.47602(3)	0.33507(3)	0.35190(5)	0.00583(6)	4.016
*Si*d	Si	1	0.85708(3)	0.33515(3)	0.35308(5)	0.00584(6)	4.025
*Si*e	Si	1	0.66352(3)	0.14148(3)	0.35247(5)	0.00588(6)	4.027
*Si*f	Si	1	0.47589(3)	0.14180(3)	0.35261(5)	0.00587(6)	4.020
*Y*a	Al	0.366(3)	0.60366(2)	0.39553(2)	–0.01702(3)	0.00932(7)	2.354
	Fe	0.634(3)	0.60366(2)	0.39553(2)	–0.01702(3)	0.00932(7)	
*Y*b	Al	0.363(3)	0.79148(2)	0.39597(2)	–0.01564(3)	0.00883(6)	2.558
	Fe	0.637(3)	0.79148(2)	0.39597(2)	–0.01564(3)	0.00883(6)	
*Y*c	Al	0.399(3)	0.60335(2)	0.20827(2)	–0.01624(3)	0.00912(7)	2.308
	Fe	0.601(3)	0.60335(2)	0.20827(2)	–0.01624(3)	0.00912(7)	
*Z*a	Al	0.953(3)	0.63171(3)	0.70363(3)	0.29762(5)	0.00621(11)	2.892
	Fe	0.047(3)	0.63171(3)	0.70363(3)	0.29762(5)	0.00621(11)	
*Z*b	Al	0.960(3)	0.96270(3)	0.70130(3)	0.63114(5)	0.00604(11)	2.894
	Fe	0.040(3)	0.96270(3)	0.70130(3)	0.63114(5)	0.00604(11)	
*Z*c	Al	0.934(3)	1.07095(3)	0.70356(3)	0.29759(5)	0.00629(10)	2.843
	Fe	0.066(3)	1.07095(3)	0.70356(3)	0.29759(5)	0.00629(10)	
*Z*d	Al	0.811(3)	0.73780(2)	0.70139(2)	0.63033(4)	0.00677(9)	2.659
	Fe	0.189(3)	0.73780(2)	0.70139(2)	0.63033(4)	0.00677(9)	
*Z*e	Al	0.964(3)	0.96241(3)	0.26211(3)	0.63122(5)	0.00608(11)	2.913
	Fe	0.036(3)	0.96241(3)	0.26211(3)	0.63122(5)	0.00608(11)	
*Z*f	Al	0.929(3)	0.96511(3)	0.59553(3)	–0.03573(5)	0.00621(10)	2.840
	Fe	0.071(3)	0.96511(3)	0.59553(3)	–0.03573(5)	0.00621(10)	
*B*1	B	1	0.77933(11)	0.89017(10)	0.4712(2)	0.00774(19)	2.963
*B*2	B	1	0.77625(10)	0.55377(10)	–0.1905(2)	0.00776(19)	2.966
*B*3	B	1	0.10989(10)	0.88943(10)	0.4761(2)	0.00776(19)	2.967
O1a	O	0.64(3)	0.66564(12)	0.33260(13)	0.13163(19)	0.0309(4)	1.236
F1a	F	0.36(3)	0.66564(12)	0.33260(13)	0.13163(19)	0.0309(4)	
O2a	O	1	0.54368(8)	0.27197(9)	–0.16428(15)	0.01388(19)	1.982
O2b	O	1	0.72711(9)	0.27113(9)	–0.16167(15)	0.01311(18)	2.011
O2c	O	1	0.72793(9)	0.45593(8)	–0.16350(15)	0.01340(18)	2.044
O3a	O	1	0.53209(8)	0.46779(8)	–0.13486(14)	0.01266(17)	1.119
H3a	H	1	0.5388(19)	0.4640(19)	–0.253(4)	0.015	
O3b	O	1	0.86882(10)	0.73373(10)	0.52987(15)	0.0156(2)	1.118
H3b	H	1	0.8775(19)	0.746(2)	0.409(4)	0.019	
O3c	O	1	0.93420(9)	0.46741(8)	–0.13587(14)	0.01305(18)	1.142
H3c	H	1	0.9310(19)	0.4665(19)	–0.254(4)	0.016	
O4a	O	1	0.75845(7)	0.51964(8)	0.42009(14)	0.01081(16)	2.036
O4b	O	1	0.48010(8)	0.24062(7)	0.42261(14)	0.01061(16)	2.039
O4c	O	1	0.75707(8)	0.24105(7)	0.42044(14)	0.01098(16)	2.049
O5a	O	1	0.57346(7)	0.42544(7)	0.44156(14)	0.01082(16)	1.976
O5b	O	1	0.57262(7)	0.14753(8)	0.44368(14)	0.01087(16)	1.974
O5c	O	1	0.85005(8)	0.42598(7)	0.44215(14)	0.01049(15)	1.984
O6a	O	1	0.86365(8)	0.52161(8)	0.13035(13)	0.00953(15)	2.006
O6b	O	1	0.65550(8)	0.52024(7)	0.12910(13)	0.00924(15)	1.977
O6c	O	1	0.65594(8)	0.13585(7)	0.13063(13)	0.00912(15)	1.965
O6d	O	1	0.86400(8)	0.34366(8)	0.13134(13)	0.00912(15)	2.011
O6e	O	1	0.47859(8)	0.34248(8)	0.13003(13)	0.00951(15)	1.958
O6f	O	1	0.48031(8)	0.13874(8)	0.13137(13)	0.01108(16)	1.937
O7a	O	1	0.66432(8)	0.61744(7)	0.42875(14)	0.01048(15)	1.984
O7b	O	1	0.95017(7)	0.61814(7)	0.43266(13)	0.00907(15)	1.970
O7c	O	1	0.66663(8)	0.04934(7)	0.43268(14)	0.00971(15)	1.970
O7d	O	1	0.38044(7)	0.04865(7)	0.43043(13)	0.00882(14)	1.977
O7e	O	1	0.38104(7)	0.33331(7)	0.43127(13)	0.00923(15)	1.987
O7f	O	1	0.94812(8)	0.33162(8)	0.43604(14)	0.01029(15)	1.976
O8a	O	1	0.87555(7)	0.60366(8)	–0.20605(15)	0.01057(15)	1.945
O8b	O	1	1.06094(7)	0.79018(7)	0.46340(15)	0.01073(16)	1.962
O8c	O	1	1.20888(7)	0.93929(7)	0.46216(14)	0.01028(15)	1.960
O8d	O	1	0.72997(8)	0.79163(7)	0.45430(16)	0.01246(17)	1.965
O8e	O	1	1.06320(8)	0.60691(7)	0.12676(15)	0.01121(16)	1.957
O8f	O	1	0.05962(8)	0.26961(8)	0.46655(15)	0.01178(16)	1.967

ponents at ~14200 and 13100 cm^{-1}, and the absorption band at lower energy is composed of components at 9100 and 8300 cm^{-1}. This observed splitting of each of the two bands at ~14000 and ~9000 cm^{-1} is due to the fact that they are both caused by electronic transitions involving Fe^{2+} at *Y*-sites as well as *Z*-sites (e.g., Smith 1978; Mattson and Rossman 1987; Taran et al. 1993; Bosi et al. 2015b). The broad and strong absorption band at 22700 cm^{-1} is caused by Fe^{2+}–Ti^{4+} charge transfer (CT) processes (e.g., Taran et al. 1993). The weak bands at 20600 and 18000 cm^{-1} are due to electronic transitions in Fe^{3+} pairs at neighboring *Y*-sites (Mattson and Rossman 1984). Additional sharp absorption bands that were observed in the **E** || **c**-spectrum in the range 6700–7000 cm^{-1} represent overtones of the fundamental (OH)-stretching modes. Comparison of the **E** ⊥ **c**-spectra of the optically uniaxial core and the optically biaxial rim (Fig. 5) shows a distinct decrease in intensity of the absorption bands at ~14000 and ~9000 cm^{-1} for the rim. As the intensities of these two bands are proportional to the $[Fe^{2+}]$*$[Fe^{3+}]$ concentration product in the sample, one can conclude that the $[Fe^{2+}]$*$[Fe^{3+}]$ value in the crystal rim is only 75% of that of the crystal core. From this observation, in combination with the EMP data for the rim and the Fe^{3+}/Fe_{tot} ratio for the crystal core as determined by the Mössbauer spectroscopy, it gives 13.92 wt. % FeO and 1.53 wt. % Fe_2O_3 for the rim. Consequently, the Fe^{3+}/Fe_{tot}-ratio in the crystal rim is 0.089 as compared to a ratio of 0.136 in the crystal bulk (from Mössbauer), which is mainly represented by the core composition.The much darker brown color of the crystal rim

(Fig. 1) results from its higher concentration of Fe^{2+} and Ti^{4+}. The intensified color is explained by a much stronger Fe^{2+}–Ti^{4+} charge-transfer (CT) band at ca. 22700 cm^{-1} in the spectrum of the rim (Fig. 5). According to the EMP data for TiO_2 and FeO in combination with optical absorption spectroscopy (for the rim) and Mössbauer spectroscopy (for the core), the $[Fe^{2+}]*[Ti^{4+}]$ concentration product is ~4.5 times higher in the rim as compared to the core. The result for the rim spectrum is an absorbance for the Fe^{2+}–Ti^{4+} CT band at ca. 22700 cm^{-1} that is offscale, although the measured tourmaline crystal is only 36 μm thick.

Tab. 4 Continued

Site *R3m*	Atom	*s.o.*	*x/a*	*y/b*	*z/c*	U_{eq}	*B.V.S.*
X	Na	1.02(1)	0.000000	0.000000	0.2344(3)	0.0263(5)	0.893
Y	Fe	0.626(4)	0.12503(2)	0.06252(2)	0.63132(4)	0.00913(7)	2.441
	Al	0.374(4)	0.12503(2)	0.06252(2)	0.63132(4)	0.00913(7)	
Z	Al	0.928(3)	0.29883(2)	0.26194(2)	0.61186(4)	0.00628(7)	2.854
	Fe	0.072(3)	0.29883(2)	0.26194(2)	0.61186(4)	0.00628(7)	
Si	Si	1	0.19170(2)	0.18984(2)	–0.00023(4)	0.00587(5)	4.037
B	B	1	0.11028(5)	0.22056(11)	0.4553(2)	0.00776(19)	2.972
O1	O	0.496(7)	0.000000	0.000000	0.7790(4)	0.0321(9)	1.164
F1	F	0.496(7)	0.000000	0.000000	0.7790(4)	0.0321(9)	
O2	O	1	0.06137(4)	0.12273(8)	0.48441(17)	0.01353(19)	1.932
O3	O	1	0.26791(11)	0.13396(5)	0.51187(16)	0.01382(19)	1.112
H3	H	1	0.260(3)	0.1298(13)	0.400(5)	0.017	
O4	O	1	0.09258(5)	0.18517(9)	0.06866(16)	0.01088(16)	2.046
O5	O	1	0.18489(9)	0.09245(5)	0.08995(16)	0.01068(16)	1.988
O6	O	1	0.19700(6)	0.18729(6)	0.77805(10)	0.00958(11)	1.974
O7	O	1	0.28428(6)	0.28471(5)	0.07948(11)	0.00963(11)	1.982
O8	O	1	0.20943(6)	0.27010(6)	0.44230(12)	0.01141(12)	1.966

4.2. Determination of number of atoms per formula unit (apfu)

In agreement with the structure-refinement results, the boron content was assumed to be stoichiometric (B^{3+} = 3.000 *apfu*). Both the site-scattering (see Hawthorne et al. 1995 for the definition of site-scattering and site-populations) and the bond lengths of *B* and *T* are consistent with the *B* site fully occupied by B and no B at the *T* site (e.g., Bosi and Lucchesi 2007). The oxidation state of iron was determined by the MS and OAS in the core and rim, respectively, of the tourmaline crystal. All Mn was considered as Mn^{2+}. In accordance with Pesquera et al. (2016), the Li_2O content was assumed to be insignificant as MgO > 2 wt. % is contained in the sample studied. The (OH) content and the *apfu* were then calculated based on 31 anions and by charge balance with the assumption (*Y* + *Z*) = 9.000 *apfu* since the SiO_2 content was assumed to be equal to 6.000 *apfu*. It is worth noting that the calculated and measured SiO_2 values are practically the same within the standard uncertainty (Tab. 1).

4.3. Single-crystal X-ray diffraction and chemical formula

With regard to the site populations at *X*, *B*, *T*, O3 (≡ V) and O1 (≡ W), the standard site preference suggested for tourmaline (e.g., Henry et al. 2011) were actually satisfied, while the *Y* and *Z* site populations were optimized according to the procedure of Wright et al. (2000) in which the default setting was assumed, but the chemical variability was constrained by electroneutrality. The resulting empirical chemical formula, with the appropriate grouping of sites, for the optically biaxial rim of the Langesundsfjord tourmaline is:

$^{X}(Na_{0.98}K_{0.01}\square_{0.01})_{\Sigma 1.00}\ ^{Y}(Fe^{2+}_{1.53}Al_{0.68}Mg_{0.35}Ti_{0.20}Fe^{3+}_{0.20}Mn_{0.02}V_{0.01}Zn_{0.01})_{\Sigma 3.00}\ ^{Z}(Al_{5.10}Fe^{2+}_{0.50}Mg_{0.40})_{\Sigma 6.00}\ (Si_6O_{18})\ (BO_3)_3\ (OH)_3\ [(OH)_{0.39}F_{0.22}O_{0.39}]_{\Sigma 1.00}$.

The calculated site-scattering from EMPA data (*X* 10.97 *epfu*, *Y* 63.37 *epfu*, *Z* 84.03 *epfu*) accords with the refined site-scattering (*X* 11.41 *epfu*, *Y* 63.34 *epfu*, *Z* 83.84 *epfu*). The detailed *Y* and *Z* site populations in the *R*1 model are reported in Tab. 6. The related weighted bond-valence sums, using Gagnè and Hawthorne (2015) parameters, are reported in Tab. 4.

The order of about 0.50 *apfu* of Fe^{2+} at the *Z* sites comes from the structure refinement of the *R*1 model that showed that one out of 6 independent *Z* sites (labeled as *Z*d) shows higher refined site scattering (15.5 *eps vs.* mean 13.7(2) *eps* for the other 5 sites), as well as longer, mean bond length (1.969 Å *vs*. 1.927(6) Å for the other 5 sites, Tab. 5) and larger octahedral-angle variance value (OAV, after Robinson et al. 1971; 53.44° *vs*. 42(3)°, Tab. 5). All these features support the local order of Fe^{2+} at the *Z*d site, and optical absorption spectra support this order. Some Fe^{2+} is ordered preferentially at *Z*f but to a lesser extent than at *Z*d (almost 1/3 of *Z*d; Tab. 6).

A less pronounced order of Al at the *Y*c site was also observed: lower refined scattering, mean bond length, and OAV than the other two *Y* sites is observed at *Y*c site (Tabs 4 and 5). This site shares one edge with the *Z*d site and another with *Z*f, where Fe^{2+} is preferentially ordered in *Z* sites. There is prominent order of Fe^{3+} and Ti^{4+} at the *Y*b site. Incident bond-valence values are within 1.93 and 2.05 valence units (*v.u.*) at all anion sites of the *R*1 model, but for O1 and O3(a,b,c), which shows values of 1.24 *v.u.* and 1.12–1.14 *v.u.*, respectively, in agreement with the presence of limited O^{2-} at O1 and only (OH) groups at O3 sites. In line with short-range bond-valence constraints around the O1 (≡W) site (e.g., Bosi 2011), the

Tab. 5 Selected interatomic distances (Å) and angle distortion parameters.

					*R*1						*R*3*m*	
*Si*a–	O6a	1.6090(10)	*Si*b–	O7a	1.6036(11)	*Si*c–	O7e	1.6080(10)	*Si*–	O7	1.6069(8)	
	O7b	1.609(2)		O6b	1.6083(10)		O6e	1.6111(11)		O6	1.6061(8)	
	O4a	1.6291(11)		O4a	1.6298(11)		O4b	1.6277(11)		O4	1.6280(5)	
	O5c	1.6429(11)		O5a	1.644(2)		O5a	1.644(2)		O5	1.6418(5)	
Mean		1.6225	Mean		1.6214	Mean		1.6226	Mean		1.6207	
TAV	(°²)	8.269	TAV	(°²)	8.648	TAV	(°²)	8.984	TAV	(°²)	8.549	
*Si*d–	O7f	1.6042(11)	*Si*e–	O7c	1.6085(11)	*Si*f–	O6f	1.6034(10)				
	O6d	1.6084(10)		O6c	1.6085(10)		O7d	1.612(2)				
	O4c	1.631(2)		O4c	1.627(2)		O4b	1.6296(11)				
	O5c	1.6442(11)		O5b	1.6425(11)		O5b	1.6444(11)				
Mean		1.6221	Mean		1.6217	Mean		1.6224				
TAV	(°²)	8.962	TAV	(°²)	9.209	TAV	(°²)	7.731				
*Y*a–	O1a	2.0388(19)	*Y*b–	O1a	2.043(2)	*Y*c–	O1a	2.031(2)	*Y*–	O1	2.0349(15)	
	O6b	2.0352(15)		O6a	2.0451(19)		O6f	2.0156(18)		O6	2.0186(8)	
	O6e	2.0386(16)		O6d	2.0383(12)		O6c	2.0391(12)		O6	2.0187(8)	
	O2c	2.0196(18)		O2c	2.0196(14)		O2a	2.0186(14)		O2	2.0340(8)	
	O2a	2.0218(18)		O2b	2.0303(18)		O2b	2.0117(18)		O2	2.0340(8)	
	O3a	2.1686(15)		O3c	2.161(2)		O3b	2.146(2)		O3	2.1600(14)	
Mean		2.0537	Mean		2.0562	Mean		2.0436	Mean		2.0500	
OAV	(°²)	79.728	OAV	(°²)	79.439	OAV	(°²)	70.690	OAV	(°²)	77.053	
*Z*a–	O8d	1.882(2)	*Z*b–	O8a	1.8957(19)	*Z*c–	O8b	1.8989(11)	*Z*–	O8	1.8993(8)	
	O7a	1.9483(12)		O7b	1.8992(11)		O8e	1.9350(11)		O8	1.9370(9)	
	O6d	1.8872(12)		O6c	1.8879(12)		O7c	1.9028(11)		O7	1.9019(8)	
	O7d	1.9000(11)		O8b	1.9313(19)		O6e	1.8931(12)		O6	1.8914(8)	
	O8c	1.9397(19)		O7e	1.9622(12)		O7b	1.979(2)		O7	1.9726(8)	
	O3c	1.9880(13)		O3b	1.9616(14)		O3a	1.987(3)		O3	1.9869(6)	
Mean		1.9241	Mean		1.9230	Mean		1.9326	Mean		1.9315	
OAV	(°²)	38.606	OAV	(°²)	42.178	OAV	(°²)	44.458	OAV	(°²)	43.556	
*Z*d–	O8f	1.9314(12)	*Z*e–	O7f	1.8812(11)	*Z*f–	O6a	1.8857(18)	O3–	H3	0.81(3)	
	O6f	1.9258(18)		O8f	1.9129(11)		O7e	1.9026(15)				
	O7a	1.9358(15)		O6b	1.8853(11)		O8e	1.8986(11)				
	O8d	1.9759(12)		O8c	1.8971(11)		O8a	1.9455(11)				
	O7f	2.0189(14)		O7d	1.962(2)		O7c	1.9780(13)				
	O3b	2.0264(15)		O3a	1.986(2)		O3c	1.9910(14)				
Mean		1.9689	Mean		1.9208	Mean		1.9336				
OAV	(°²)	53.440	OAV	(°²)	39.069	OAV	(°²)	45.639				
B1–	O8d	1.373(2)	*B2*–	O8f	1.3754(19)	*B3*–	O8b	1.380(2)	*B*–	O8 ×2	1.3772(11)	
	O8e	1.3815(19)		O8a	1.382(2)		O8c	1.377(2)				
	O2a	1.375(2)		O2c	1.371(2)		O2b	1.371(2)		O2	1.3718(19)	
Mean		1.3764	Mean		1.3763	Mean		1.3761	Mean		1.3754	
			*Na*1–	O2c	2.4803(18)							
				O2a	2.4800(18)							
				O2b	2.4910(15)				*Na*1–	O2 ×3	2.4815(19)	
				O5c	2.746(3)							
				O5a	2.7761(19)					O5 ×3	2.7666(14)	
				O5b	2.8006(18)							
				O4c	2.782(3)					O4 ×3	2.8316(15)	
O3a–	H3a	0.81(3)		O4b	2.855(3)				Mean		2.6932	
O3b–	H3b	0.89(3)		O4a	2.848(3)							
O3c–	H3c	0.86(3)	Mean		2.6954				O3–	H3	0.81(3)	

Note: *TAV* and *OAV* = tetrahedral and octahedral angle variance by Robinson et al. (1972)

amount of calculated O^{2-} can be locally related to the presence of Al^{3+}–Ti^{4+}–Al^{3+} or Al^{3+}–Fe^{3+}–Al^{3+} triplets at the *Y*a–*Y*b–*Y*c sites, ca. 38% of probability (with some Al^{3+} at *Y*a being substituted by Fe^{3+} or V^{3+}). Fluorine is probably related to Fe^{2+}–Mg^{2+}–Fe^{2+} triplets.

5. Discussion

Previous studies report optically anomalous tourmaline with biaxial character, which is incompatible with its putative *R*3*m* symmetry. The optically zoned tourmaline crystal has the chemical composition of schorl in the core and the rim: the former is slightly richer in Al, Fe^{3+} and O^{2-}, whereas the latter is somewhat richer in Ti, Mg, F and Fe^{2+} (Tab. 1).

Regarding the rim zone, the results of structure refinement with an *R*1 model show preferential order of Fe^{2+} at the *Z*d and *Z*f sites, and Fe^{3+} and Ti^{4+} order at the *Y*b site, in accord with the spectroscopic results. Interestingly, order at the *Z* sites occurs in alternating fashion along [110], breaking the symmetry of the 3*Y*–6*Z* cluster (Fig. 6). This is related to the observed ellipticity of the optical indicatrix in the *Z*–*Y* plane and its relative orientation to the crystallographic axes of the triclinic cell. Order is ascribed to preferential selectivity at the growing surface of the prism. Positions related by symmetry in the bulk of a crystal may be structurally and energetically non-equivalent on a growing surface. These differences lead to an ordered distribution of structural units on the surface that remains metastably included in the structure as the crystal growths if diffusion is too slow. The crystal's symme-

try is reduced, which leads to anomalous birefringence. This is the cause for anomalous optical properties claimed in elbaite following Shtukenberg et al. (2007) and Hughes et al. (2011) and it is very likely the cause for the sample of this study.

Nominally uniaxial crystals (trigonal space group *R*3*m*) often exhibit biaxiality with the axial angle attaining values of 5–10° or even 30° (Shtukenberg et al. 2007). Natural polychrome tourmalines are in fact, characterized by relative:

– small optical axial angles, which are mainly stress-induced optical anomalies;
– large optical axial angles, which are due to growth ordering of atoms induced optical anomalies.

The value obtained for the studied sample is more in agreement with growth ordering. The observed elongation of the *Z*d-octahedron is along a direction that forms an angle of ca. 73° with the a unit-cell edge and coincides with the direction for γ-refraction index (Fig. 6). The γ-refraction index is also perpendicular to the growth direction of the prism face. A similar orientation of the slow-length axis of the indicatrix has been described very recently in sector-zoned garnet crystals from Port Macquarie (Australia) by Cesare et al. (2022), showing anomalous birefringence by using polychromatic polarizing microscopy (Shribak 2015, 2017). This technique allows elucidation of a very subtle variation of the retardation at low birefringence. It is also sensitive to the apparent orientation of the elongation of the optical indicatrix through the different polarization of the wavelengths comprised in white light. In Fig. 2d of Cesare et al. (2022), it is clearly shown that the slow length is along the growing direction. Although this is interpreted by Cesare et al. (2019) as due to a desymmetrization due to cubic to tetragonal change, it might well be related to the kinetic ordering of atoms during the growing of the garnet crystals (probably due to ordering of Fe^{2+} at the *Y* site in the garnet structure) being perhaps related to cyclic chemical zonation along the growing front. We suggest a similar process for the schorl studied here.

Tab. 6 Site assignments on the basis of observed site-scatterings and bond-valence sums.

Site	Occupants	Observed site-scattering (e^-)	Calculated mean bond length (Å)
Ya	$Fe^{2+}_{0.604}Al_{0.305}Mg_{0.052}Fe^{3+}_{0.029}V^{3+}_{0.011}$	21.26(4)	2.054
Yb	$Fe^{2+}_{0.327}Mg_{0.274}Ti^{4+}_{0.207}Fe^{3+}_{0.169}Mn^{2+}_{0.023}$	21.31(4)	2.053
Yc	$Fe^{2+}_{0.597}Al_{0.371}Mg_{0.025}Zn_{0.007}$	20.79(4)	2.044
Za	$Al_{0.898}Fe^{2+}_{0.053}Mg_{0.049}$	13.64(4)	1.924
Zb	$Al_{0.900}Mg_{0.054}Fe^{2+}_{0.047}$	13.55(4)	1.923
Zc	$Al_{0.854}Fe^{2+}_{0.074}Mg_{0.072}$	13.89(4)	1.933
Zd	$Al_{0.681}Fe^{2+}_{0.201}Mg_{0.119}$	15.49(4)	1.969
Ze	$Al_{0.916}Fe^{2+}_{0.042}Mg_{0.042}$	13.50(4)	1.921
Zf	$Al_{0.852}Fe^{2+}_{0.079}Mg_{0.069}$	13.96(4)	1.934

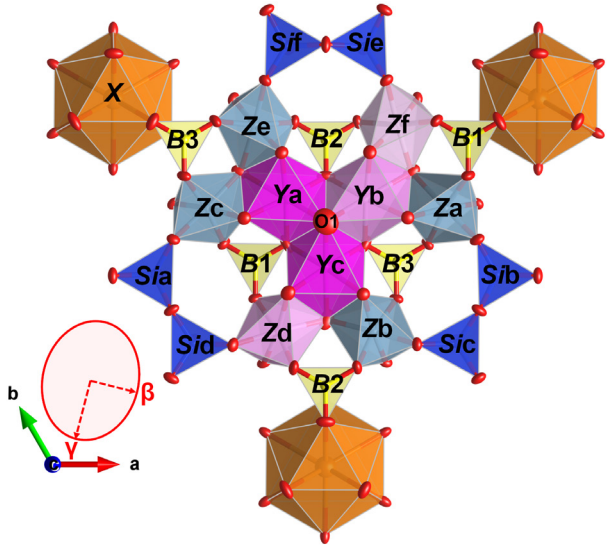

Fig. 6 The crystal structure projected onto [001] showing the order at the *Y* sites. Atoms drawn as ellipsoids at 90% probability. *T* sites in blue; Al-dominant at sites in cyan; *B* sites in yellow; Fe^{2+} -dominant sites in purple; Na sites in light brown; oxygen anion on sites in red. The saturation of the hue is related to the dominant cation. The orientation of the γ–β section of the optical indicatrix is shown with the orientation from optical measurements (see text). Obtained with Vesta 3 (Momma and Izumi 2011).

Our results clearly support a lowering of symmetry in our tourmaline sample that is compatible with triclinic symmetry due to Fe^{2+} order along particular crystallographic directions. This order seems to be the cause of a slower vibrating direction leading to the ellipticity of the optical indicatrix: it should have a circular section perpendicular to in a uniaxial crystal but becomes elliptic with ω' > ω and ω' becoming γ, whereas ε becomes α, in agreement with a negative sign (–) of the optical indicatrix of trigonal tourmaline. Our sample is triclinic but has the same structure topology as trigonal tourmaline, it should be designated as schorl-1*A* (Nickel and Grice 1998). Similarly, schorl exhibiting monoclinic symmetry would be termed schorl-1*M*.

6. Conclusions

A single crystal of schorl composition from Langesundsfjord (Norway) shows different crystallographic symmetry, accompanied by a different optical behavior: trigonal (*R*3*m*) and uniaxial in the dark brownish core and triclinic (*R*1) and biaxial in the darker brownish rim. Anomalous optical behavior, related to triclinic structure, is due to the preferential ordering of Fe^{2+} at one of the non-equivalent 6 *Z* sites.

Some schorl samples from the Langesundsfjord area, named as *luinaite-(OH)* and reported as monoclinic (*Cm*) by Kolitsch et al. (2013), should be best termed as schorl-1*M*. Consequently, it can be concluded that trigonal, monoclinic, and triclinic schorl samples may occur in Langesundsfjord area. Our study indicates that even in the presence of excellent statistical residual factors from excellent X-ray diffraction data, the lowering of symmetry due to cation ordering may have been overlooked in many other tourmaline samples in the absence of an opportune check of the optical behavior.

Acknowledgments. Chemical analyses were done with the kind assistance of M. Serracino to whom the authors express their gratitude. F.C. acknowledges financial support by the grant Ricerca Locale 2019, Università di Milano and from the Italian Ministry of Education (MIUR) through the project "Dipartimenti di Eccellenza 2018–2022". Funding by Sapienza University of Rome (Prog. Università 2020 to F.B.) is gratefully acknowledged. Careful reviews by Frank Hawthorne and John Hughes are appreciated.

Electronic supplementary material. The crystallographic information files (CIF) are available online on the Journal website (*http://dx.doi.org/10.3190/jgeosci.344*).

References

Akizuki M (1981) Origin of optical variation in analcime. Am Mineral 66: 403–409

Akizuki M (1984) Origin of optical variations in grossular-andradite garnet. Am Mineral 66: 403–409

Allen FM, Buseck PR (1988) XRD, FTIR and TEM studies of optically anisotropic grossular garnets. Amer Miner 73: 568–584

Andersen T, Erambert M, Larsen AO, Selbekk RS (2010) Petrology of nepheline syenite pegmatites in the Oslo Rift, Norway: Zirconium silicate mineral assemblages as indicators of alkalinity and volatile fugacity in mildly agpaitic magma. J Petrol 51: 2303–2325

Andrut M, Wildner M, Beran A (2002) The crystal chemistry of birefringent natural uvarovites. Part IV. OH defect incorporation mechanisms in non-cubic garnets derived from polarized IR spectroscopy. Eur J Mineral 14: 1019–1026

Antao SM (2013) The mystery of birefringent garnet: is the symmetry lower than cubic? Powder Diffr 28: 265–272

Bosi F (2011) Stereochemical constraints in tourmaline: from a short-range to a long-range structure. Canad Mineral 49: 17–27

Bosi F, Lucchesi S (2007) Crystal chemical relationships in the tourmaline group: structural constraints on chemical variability. Amer Miner 92: 1054–1063

Bosi F, Skogby H, Lazor P, Reznitskii L (2015a) Atomic arrangements around the O3 site in Al- and Cr-rich oxy-tourmalines: a combined EMP, SREF, FTIR and Raman study. Phys Chem Miner 42: 441–453

Bosi F, Andreozzi GB, Hålenius U, Skogby H (2015b) Experimental evidence for partial Fe^{2+} disorder at the *Y* and *Z* sites of tourmaline: a combined EMP, SREF, MS, IR and OAS study of schorl. Mineral Mag 79: 515–528

Bosi F, Skogby H, Balić-Žunić T (2016) Thermal stability of extended clusters in dravite: a combined EMP, SREF and FTIR study. Phys Chem Miner 43: 395–407

Bosi F, Skogby H, Hålenius U, Ciriotti ME, Mills SJ (2022): Lowering *R*3*m* Symmetry in Mg–Fe-tourmalines: the crystal structures of triclinic schorl and oxy-dravite, and the mineral luinaite-(OH) discredited. Minerals 12: 430

Brauns R (1891) Optischen Anomalien der Krystalle. Bey S. Hirzel, Leipzig (in German)

Brøgger WC (1890) Die mineralien der syenitpegmatitgänge der Südnorwegischen augit- und nephelinesyenite. Z Kristallogr Mineral 16: 1–663 (in German)

Campomenosi N, Mazzucchelli ML, Mihailova BD, Angel RJ, Alvaro M (2020) Using polarized Raman spectroscopy to study the stress gradient in mineral systems with anomalous birefringence. Contrib Mineral Petrol 175: 1–16

Cesare B, Nestola F, Johnson T, Mugnaioli E, Della Ventura G, Peruzzo L, Bartoli O, Viti C, Erickson T (2019) Garnet, the archetypal cubic mineral, grows tetragonal. Sci Rep 9: 14672

Cesare B, Campomenosi N, Shribak M (2022) Polychromatic polarization: Boosting the capabilities of the good old petrographic microscope. Geology 50: 137–141

Foord EE, Cunningham CG (1978) Thermal transformation of anomalously biaxial dimetric crystals. Amer Miner 63: 747–749

Foord EE, Mills BA (1978) Biaxiality in 'isometric' and 'dimetric' crystals. Amer Miner 63: 316–325

Gagnè OC, Hawthorne FC (2015) Comprehensive derivation of bond-valence parameters for ion pairs involving oxygen. Acta Crystallogr B71: 562–578

Gonzalez-Carreño T, Fernández M, Sanz J (1988) Infrared and electron microprobe analysis of tourmaline. Phys Chem Miner 15: 452–460

Grifen DT, Hatch DM, Phillips WR, Kulaksiz S (1992) Crystal chemistry and symmetry of a birefringent tetragonal pyralspite75–grandite25 garnet. Amer Miner 77: 399–406

Hariya Y, Kimura M (1978) Optical anomaly garnet and its stability field at high pressures and temperatures. J Fac Sci, Hokkaido Univ, Ser IV, 18: 611–624

Hawthorne FC, Ungaretti L, Oberti R (1995) Site populations in minerals; terminology and presentation of results of crystal-structure refinement. Canad Mineral 33(4): 907–911

Henry DJ, Novák M, Hawthorne FC, Ertl A, Dutrow BL, Uher P, Pezzotta F (2011) Nomenclature of the tourmaline-supergroup minerals. Amer Miner 96: 895–913

Hofmeister AM, Schaal RB, Campbell KR, Berry SL, Fagan TJ (1988) Prevalence and origin of birefringence in 48 garnets from the pyrope–almandine–grossularite–spessartine quaternary. Amer Miner 83: 1293–1301

Howell D (2012) Strain-induced birefringence in natural diamond: a review. Eur J Mineral 24: 575–585

Hughes JM, Rakovan J, Ertl A, Rossman GR, Baksheev I, Bernhardt H-J (2011) Dissymmetrization in tourmaline: the atomic arrangement of sectorally zoned triclinic Ni-bearing dravite. Canad Mineral 49: 29–40

Isogami M, Sunagawa I (1975) X-ray topographic study of a topaz crystal. Amer Miner 60: 889–897

Kolitsch U, Husdal TA, Brandstätter F, Ertl A (2011) New crystal-chemical data for members of the tourmaline group from Norway: occurrences of fluor-schorl and luinaite-(OH). Norsk Bergverksmuseet Skrift 46: 17–24

Kolitsch U, Andresen P, Husdal TA, Ertl A, Haugen A, Ellingsen HV, Larsen AO (2013) Tourmaline-group minerals from Norway, part II: occurrences of luinaite-(OH) in Tvedalen, Larvik and Porsgrunn, and fluor-liddicoatite, fluor-elbaite and fluor-schorl at Ågskardet, Nordland. Norsk Bergverksmuseums Skrift 50: 23–41

Madelung A (1883) Beobachtungen mit Brethaupt's Polarisationmikroskop. Z Kristallogr 7: 73–76

Mattson SM, Rossman GR (1984) Ferric iron in tourmaline. Phys Chem Miner 11: 225–234

Mattson SM, Rossman GR (1987) Fe^{2+}–Fe^{3+} interactions in tourmaline. Phys Chem Miner 14: 163–171

Momma K, Izumi F (2011) VESTA 3 for three-dimensional visualization of crystal, volumetric, and morphology data. J Appl Cryst 44: 1272–1276

Nickel EH, Grice JD (1998) The IMA Commission on New Minerals and Mineral Names; procedures and guidelines on mineral nomenclature, 1998. Canad Mineral 36: 913–926

Pesquera A, Gil-Crespo PP, Torres-Ruiz F, Torres-Ruiz J, Roda-Robles E (2016) A multiple regression method for estimating Li in tourmaline from electron microprobe analyses. Mineral Mag 80: 1129–1133

Pouchou JL, Pichoir F (1991) Quantitative analysis of homogeneous or stratified microvolumes applying the model "PAP". In: Heinrich KFJ, Newbury DE (Eds) Electron Probe Quantitation, Pp. 31–75, Plenum, New York

Prescher C, McCammon C, Dubrowinsky L (2012) MossA: a program for analyzing energy-domain Mössbauer spectra from conventional and synchrotron sources. J Appl Crystallogr 45: 329–331

Robinson K, Gibbs GV, Ribbe PH (1971) Quadratic elongation: a quantitative measure of distortion in coordination polyhedra. Science 172: 567–570

Sheldrick GM (2015) Crystal Structure refinement with SHELX. Acta Crystallogr C71: 3–8

Shribak M (2015) Polychromatic polarization microscope: Bringing colors to a colorless world. Sci Rep 5: 17340

Shribak M (2017) Polychromatic polarization state generator and its application for real-time birefringence imaging: US Patent 9625369, International Class G01N 21/2

Shtukenberg A, Rozhdestvenskaya I, Frank-Kamenetskaya O, Bronzova J, Euler H, Kirfel A, Bannova I, Zolotarev A (2007) Symmetry and crystal structure of biaxial elbaite-liddicoatite tourmaline from the Transbaikalia region, Russia. Amer Miner 92: 675–686

Smith G (1978) A reassessment of the role of iron in the 5,000–30,000 cm^{-1} region of the electronic absorption spectra of tourmaline. Phys Chem Miner 3: 343–373

Steven CJ, Gunter ME (2018) EXCELIBR: An Excel spreadsheet for solving the optical orientation of uniaxial and biaxial crystals. The Microscope 65: 147–152

Takeuchi Y, Haga N (1976) Optical anomaly and structure of silicate garnets. Proc Jap Acad 52: 228–231

Taran MN, Lebedev AS, Platonov AN (1993) Optical absorption spectroscopy of synthetic tourmalines. Phys Chem Miner 20: 209–220

Watenphul A, Burgdorf M, Schlüter J, Horn I, Malcherek T, Mihailova B (2016) Exploring the potential of Raman spectroscopy for crystallochemical analyses of complex hydrous silicates: II. Tourmalines. Amer Miner 101: 970–985

Wertheim G (1851) Note sur la double réfraction artificiellement produite dans les cristaux du système régulier. Compt Rend Acad Sci Paris 33: 576 (in French)

Wertheim G (1854) Sur la double réfraction temporairement produite dans les corps isotropes, et sur la relation entre l'élasticité mécanique et entre l'élasticité optique. Ann Chim Phys ser III 40: 156 (in French)

Wilson AJC (1992) International Tables for Crystallography, Volume C: Mathematical, physical and chemical tables. Kluwer Academic Publishers, Dordrecht, NL, pp 1–883

Wright SE, Foley JA, Hughes JM (2000) Optimization of site occupancies in minerals using quadratic programming. Amer Miner 85, 524–531